

Lawrence Berkeley National Laboratory

LBL Publications

Title

A synchrotron study of defect and strain inhomogeneity in laser-assisted three-dimensionally-printed Ni-based superalloy

Permalink

<https://escholarship.org/uc/item/0xz131cf>

Journal

Applied Physics Letters, 107(18)

ISSN

0003-6951

Authors

Li, Yao
Qian, Dan
Xue, Jiawei
et al.

Publication Date

2015-11-02

DOI

10.1063/1.4934839

Peer reviewed

1 **A synchrotron study of defect and strain inhomogeneity**
2 **in laser-assisted 3D-printed Ni-based superalloy**

3 Yao Li^{1,2}, Dan Qian², Jiawei Xue², Jingchun Wan², Anfeng Zhang^{3*},

4 Nobumichi Tamura⁴, Zhongxiao Song^{2*}, Kai Chen^{1,2,*}

51. Center for Advancing Materials Performance from the Nanoscale (CAMP-Nano),

6 State Key Laboratory for Mechanical Behavior of Materials, Xi'an Jiaotong University,

7 Xi'an, Shaanxi 710049, P.R. China

82. State Key Laboratory for Mechanical Behavior of Materials, Xi'an Jiaotong

9 University, Xi'an, Shaanxi 710049, P.R. China

103. State Key Laboratory for Manufacturing Systems Engineering, Xi'an Jiaotong

11 University, Xi'an, Shaanxi 710049, P.R. China

124. Advanced Light Source, Lawrence Berkeley National Laboratory, Berkeley,

13 California 94720, USA

14

15* Author to whom correspondence should be addressed. Email: kchenlbl@gmail.com (K.C.),

16 zhangaf@mail.xjtu.edu.cn (A.F.Z.), or zhongxiaosong@mail.xjtu.edu.cn (Z.X.S.).

17

18 **Abstract**

19 Synchrotron X-ray microdiffraction was employed to investigate the inhomogeneous

20 distribution of defect and residual strain in the transitional region between the

21 dendritic and stray grains in a laser-assisted 3D printed Ni-based superalloy. The

22 dendritic region was found to be under tensile strain transversely to the primary

23 dendrite arm directions. The dendrite edges, where high level of strains and

24geometrically necessary dislocations were detected, were discerned as low angle grain
25boundaries. High angle grain boundaries were observed in the stray grain region, and
26the orientation of the strain tensor in this region varied dramatically at the micron
27scale, in contrast with the more or less homogeneous distribution in the dendritic
28region.

29

30**Keywords:** inhomogeneous defects and strains, laser assisted 3D printing, Ni-based
31superalloy, synchrotron X-ray microdiffraction

32 Serving as the core components of aeronautical and stationary gas turbines used
33 in harsh environment, single crystal Ni-based superalloy blades are the tools of choice
34 due to their combinatory performances, which include high temperature strength,
35 good thermal anti-oxidation property, and excellent creep resistance.¹ To prolong the
36 service lifetime and reduce the overall cost, development of new restoration
37 approaches to repair the cracked or worn parts of the blades is needed, and laser
38 additive forming, better known as laser-assisted 3D printing, is considered as one of
39 the most promising methods.² In this process, the superalloy powders are continuously
40 injected into the molten pool formed by a high-intensity scanning laser beam. Once
41 the laser beam moves to the next scanning position, the melt nucleates and grows in
42 epitaxy with the single crystal substrate. However, if for some reasons the nucleation
43 density and solidification velocity exceed a critical value, numerous crystal grains will
44 grow simultaneously with random orientations, known as “stray grains”.³ The stray
45 grains are deleterious to the blade’s resistance to creep and thermal fatigue because of
46 the presence of high angle grain boundaries (HAGBs).⁴

47 It has been reported that an intrinsic strain field is generated in the conventional
48 cast Ni-based superalloy crystal during the rapid cooling procedure. From previous
49 modeling work, tensile strain exists in all three directions in the cast Ni-based
50 superalloy, which is harmful for the mechanical behaviors.⁷ Moreover, lattice misfit of
51 γ / γ' phases results from the different site substitution of refractory elements, such as
52 Ta, W, Mo in the two phases,^{5,6} and discrepancy of the relative γ / γ' volume fraction

53 is frequently detected between the dendrite core and the interdendritic region,⁷ giving
54 rise to inhomogeneous thermal contraction and strain/stress distribution, and
55 eventually favoring the disastrous nucleation of thermal fatigue cracks.⁸ However,
56 because of high solidification velocity and thermal gradient, the dendrite arrays in 3D-
57 printed superalloy are usually finer than in traditionally solidified alloys, therefore it
58 is not trivial to investigate the defect and strain distribution at the sub-dendrite scale
59 via the traditional characterization techniques which are limited by spatial or angular
60 resolution.⁴ In this Letter, we evaluate the microstrain and defect distribution near the
61 interface of the columnar dendrites and stray grains in a 3D-printed Ni-based
62 superalloy using synchrotron X-ray microdiffraction (μ XRD). Prominent defect
63 inhomogeneity and strain gradient were measured at the dendrite edges.

64 The 3D printed DZ125L superalloy, designed in China, was deposited by an
65 independently developed XJTU-I 3D printing system equipped with a Nd:YAG laser
66 with a beam size of 0.5 mm. The substrate was cut from a single crystalline DZ125L
67 superalloy cast ingot. Its surface was parallel to {001} plane, and the cross-section
68 planes were {110} planes. The powder with diameters ranging from 50 to 100 μ m
69 with similar composition was coaxially injected at a 9 mm³/s feeding speed by Ar gas
70 carrier into the molten pool formed by the laser beam with a power of 230 W and 4
71 mm/s laser scanning speed. Therefore the molten powder solidified on top of the
72 crystal and deposited layer by layer. Table I lists the chemical compositions of the
73 powder and substrate. More details about the 3D printer and the forming process can

74be found elsewhere.⁹ Figure 1(a) shows schematically the epitaxial deposition of
75columnar dendrites on a single crystalline substrate and then the transition to equiaxed
76stray grains.

77 The μ XRD experiment was carried out on Beamline 12.3.2 at the Advanced
78Light Source (ALS) in Lawrence Berkeley National Laboratory (LBNL).¹⁰ The
79sample was mounted on an **X-Y** scanning stage at a 45° tilt angle relative to the
80incident X-ray beam which has an energy bandpass of 5 to 24 keV, and the deposition
81direction was roughly parallel to the **Y**-scanning direction. A 150 × 300 μm^2 transition
82region from the columnar/cellular dendrites to stray grains was scanned with the
83micro-focused X-ray beam using a 2 μm step size and a Laue pattern was obtained at
84each step using a 1 s exposure time from an area detector (DECTRIS Pilatus 1 M)
85placed about 140 mm away from the X-ray focal point at 90° with respect to the
86incoming beam. A total number of 11250 patterns were automatically analyzed by the
87custom-made software XMAS¹¹ to obtain the crystal orientation and lattice strain at
88each scanning position. This technique provides high crystal orientation ($\sim 0.01^\circ$)¹²
89and good deviatoric strain resolution ($\sim 10^{-4}$),¹³ and the defect type and density
90distribution in the scan area can also be revealed from the shape of the diffraction
91peaks.^{14,15} In all the microstructure maps and optical figures in this Letter, the crystal
92is oriented in the same way.

93 After the μ XRD experiment, the same sample was etched using fresh nitro-
94hydrochloric acid for about 5 s for metallographic observation under an optical

95microscope. Figure 1(b) and (c) shows the typical hierarchical morphology of deposit
96microstructures of the specimen close to the area that was studied via \square XRD. In
97Figure 1(b) with lower magnification, the substrate, columnar dendrites close to **Y**
98direction, and stray grains are clearly observed from bottom to top. The rectangular
99area is magnified and shown in Figure 1(c), in which cellular grains are found
100between two adjacent columnar dendrites, probably due to the thermal effects when
101the upper layer was deposited on the lower one. The average trunk spacing between
102the primary dendrites is about 12 \square m, which is much smaller than the one in
103conventional solidification process because of the high solidification velocities and
104thermal gradient.⁴ Moreover, the inverse pole figure (IPF) map along the **Y**-axis
105obtained from the \square XRD measurements is shown in Figure 1(d) and proves that the
106growth direction of primary dendrites is almost collinear with the $\langle 001 \rangle$ direction.
107This is also confirmed by the poles (marked in red) of the dendritic region in the
108 $\{001\}$ stereographic projection of Figure 1(f), indicating epitaxial growth and single
109crystallinity. Similarly, the IPF map along the **X**-axis in Figure 1(e) and $\{110\}$
110stereographic projection in Figure 1(g) illustrate that the **X**-axis practically consists of
111the $\langle 110 \rangle$ direction in the dendritic region. Furthermore, the random scattering of the
112superjacent stray grain poles (in blue) in both Figure 1(f) and 1(g) indicate the
113absence of texture, which is attributed to numerous random nucleation sites at the
114front of dendrites. It is worth noting that some spurious grain boundaries displayed in
115the dendritic region come from failed indexation of Laue patterns due to the presence

116of impurities.

117 To emphasize the fine orientation differences in dendritic region, the
118disorientation angle between each pair of adjacent scan positions is calculated and
119plotted in Figure 2 following a method introduced in details elsewhere.¹⁶ The high
120angle ($> 5^\circ$) grain boundaries in the stray grain region are delineated in thick black
121lines, while the low angle ($< 5^\circ$) grain boundaries (LAGBs) are in gradient of light to
122dark red. Comparing with Figure 1(c), we conclude that the primary dendrite edges
123were LAGBs and that growth deviation occurs between each pair of adjacent primary
124dendrites. This observation agrees with the theoretical prediction of the extreme
125difficulty to obtain a perfect single crystal from solidification.⁴ Dendrite growth slight
126deflection from its $\langle 001 \rangle$ direction is linked to solidification kinetics, including
127thermomechanical stresses induced by σ' participation¹⁷ and surface tension by
128Marangoni convection.⁴ As a consequence, the dendritic region shows a minor
129disorientation and LAGBs spanning over a few degrees. It should be emphasized here
130that only the combination of sub-degree orientation resolution and micron-scale
131intragranular spatial resolution offered by μ XRD allows the discernment of dendrite
132edges for such 3D printed Ni-based superalloy specimens. As a comparison, a $150 \times$
133300 μm^2 area in the substrate was scanned in the similar way while with 5 μm step
134size, and disorientation distributes in the range of (0.05 ± 0.03) degree, which was
135about one order of magnitude lower than the one in the dendritic region. The
136disorientation distribution statistics of both the substrate and the dendritic region are

137 shown in Figure S1 of the supplementary online information (SOI).¹⁸

138 Generally speaking, splitting and streaking of Laue diffraction peaks can be
139 linked to the density of geometrically necessary dislocations (GNDs). From Cahn-
140 Nye relationship,¹⁹ in our case a disorientation gradient of 1 degree per micron
141 corresponds to a GND density of $\sim 7 \times 10^9 \text{ cm}^{-2}$. To evaluate the GND distribution in
142 local interdendritic regions, a single dendrite displayed in Figure 3(a) is considered
143 from the highlighted rectangular region in Figure 2. The dendrite grew with about a
144 10° inclination from the **Y**-axis. In order to study the defect types, the diffraction
145 peak shape evolution along three lines parallel to the dendrite axis is investigated,
146 including two lines near both sides of dendrite edge in pink and light blue, and one
147 line at the dendrite core in orange, respectively (shown in Figure 3(b)). For simplicity,
148 six typical 133 peaks are picked out along each line. It can be seen that the peak
149 position is changing, indicating a rotation of the dendrite arm. Besides, the peaks are
150 streaking or splitting near the dendrite edges, while remaining sharp in the dendrite
151 core, indicating an inhomogeneous distribution of GNDs within a single dendrite.
152 When comparing the crystal orientation at each scanning position along two lines
153 (purple and green) shown in Figure 2 with the first pixel of each line, it is found that
154 the rotation axis varies from dendrite to dendrite, as shown in Figure S2 in SOI.¹⁸ This
155 indicates that different slip systems are activated in different dendrites. The GNDs are
156 more prone to aggregate near the LAGBs (dendrite edges) than in the core of
157 dendrites, and the rotation axis at the dendritic boundaries are almost randomly

158oriented, which are probably attributed to the complex flux convection in the
159interdendritic region.

160 We notice in Figure 3(b) that the peak splitting/streaking is more severe at the
161dendrite root than in the middle and tips. For a more general view, the 220 peak shape
162in all the patterns recorded along two lines parallel to the interface between two layers
163of dendrite arrays were investigated. We found that all of the peaks in the middle
164(purple line in Figure 2) of the dendrite layer are sharp, while the ones near the
165dendrite root (indicated by the green line in Figure 2) are almost all streaking or
166splitting. The distributions of disorientation and calculated GND density are shown in
167Figure 3(c) by considering both the width and splitting angle of the Laue peaks in an
168individual pattern, which records the GND density mainly in the depth direction (the
169high energy X-ray penetrates Ni by up to 40 μm while the beam size is about 1×1
170 μm^2), and the disorientation angle between two adjacent patterns, which demonstrates
171mainly the GND density in the **XY**-plane. From Figure 3(c), two observations can be
172made. First, the GND density in the investigated region of the 3D-printed superalloy
173is more than one order of magnitude higher than that in a material fabricated via
174traditional solidification process, due to the higher solidification kinetics.²⁰ Second,
175the GND density near the root of the dendrite layer is significantly higher than that in
176the middle. Possible explanations include that a single dendrite can be regarded as a
177cantilever beam anchored at the position of the solidus isotherm by the interdendritic
178solid,²¹ and that when the new layer was deposited, the surface was not a perfect

179single crystal and inhomogeneous nucleation happened.²² The beam sustains bending
180moments and torques on account of the differential thermal contraction between
181dendrite and interdendritic region as a result of elemental segregation.⁷ The
182cumulative mechanical constraints compel local plastic deformation, resulting in the
183accumulation of disorientation and defect around the root of the dendrite, where high
184level of residual strain is frequently preserved.

185 To evaluate the magnitude of the residual strain, the Von Mises strain ($\epsilon_{v.m.}$)
186is calculated and displayed in Figure 4(a). The pixel/angular deviation between the
187theoretical and experimental peak positions in the Laue pattern after strain refinement
188is shown in Figure S3 of SOI.¹⁸ High residual strain and large deviation occur in the
189vicinity of dendrite edges along the LAGBs in blue lines. The magnitude of strain in
190the dendritic region is slightly lower than that in stray grain region, so the generation
191of stray grains is deleterious to the mechanical properties and high-temperature creep
192resistance of turbine blade. To illustrate the orientation of the deviatoric strain

193 (ϵ_{dev}) ellipsoid, principal strains and their axes are derived from the eigenvalues
194and eigenvectors of the strain tensor at each location. Because of the nature of
195deviatoric strain, the minimum of three eigenvalues is negative, while the maximum is
196positive, indicating compression and tension, respectively. Given this, we plot the
197compressive (blue) and tensile (red) principal strain distribution in Figure 4(b) and
1984(c), respectively, and delineate a series of arrows in every 7th pixel to denote the

199direction of principal strain axes projected on the **XY**-plane. The strain axis
200distribution in stray grain region is found to be inhomogeneous, in association with
201the random crystal orientation distribution, while the well-aligned arrows reveal
202uniform distribution of strain tensor orientation in the dendritic region. It is worth
203noting that the strains shown here are deviatoric, and thus cannot be compared with
204the full strains reported before⁷, but the relative magnitude is comparable. Vertically
205aligned compressive strain suggests that the dendrite “contract” along the dendrite
206growth direction and stretched perpendicular to the primary dendrite axis. However,
207previous modelling predicts that conventionally solidified Ni-based superalloy
208stretches in all three dimensions and it is more tensile along the dendrite growth
209direction than in the transverse direction.⁷ We postulate the difference is rooted from
210the layer-by-layer raster scanning deposition process of 3D printing. With this
211technique, each freshly deposited layer can be regarded as a free surface, so that the
212out-of-plane stress, similar to the case in thin films, is close to zero, and thus the strain
213along the primary dendrite arms is determined by the in-plane stress and has opposite
214sign to the strain transversely to the dendrite arms. While in the conventional process,
215solidification occurs continuously and the stress builds up in all three dimensions;
216therefore the out-of-plane strain could have the same sign as the in-plane ones.
217Regarding the origin of the tensile strain perpendicular to the dendrite, it is believed to
218result from the volume shrinkage during the solidification process.

219 To conclude, the defect inhomogeneity and strain gradient near the transitional

220region of columnar/cellular dendrites and stray grains in a laser-assisted 3D-printed
221Ni-based superalloy were probed with synchrotron μ XRD technique. The detailed
222profile of dendrite edges are discerned from the fine crystal orientation deviation, also
223known as LAGBs, between dendritic and interdendritic region. In addition, the
224LAGBs are the preferential sites for defects (mainly GNDs) and residual strain to
225build up, which may initiate hot cracks. The interdendritic strain can be attributed to
226the defects introduced in solidification process and the preservation of thermal stress
227caused by the contraction misfit between the dendritic and interdendritic region.
228Deviatoric strain maps show a relative compression state along the primary dendrite
229growth direction, and a more tensile state perpendicular to the primary dendrite axes.
230This is believed to be governed by the local microstructure and thermal contraction
231controlled by the composition of the superalloy and its processing parameters.
232Moreover, the strain distribution in stray grain region is much more inhomogeneous
233owing to the presence of HAGBs.

234

235**Acknowledgements:**

236This work is supported by the National Natural Science Foundation of China (Grant
237No. 51302207, 51275392, 51271140) and the Fundamental Research Funds for the
238Central Universities (Grant No. 2015gjh03). KC is supported by the National Young
2391000 Talents Program of China. The ALS is supported by the Director, Office of
240Science, Office of Basic Energy Sciences, Materials Science Division, of the U.S.

241Department of Energy under Contract No. DE-AC02-05CH11231 at LBNL.

242

243References:

- 244¹ T. M. Pollock and S. Tin, *J. Propuls. Power* **22**, 361 (2006).
- 245² R. Vilar and A. Almeida, *J. Laser Appl.* **17004**, (2015).
- 246³ S. Mokadem, C. Bezençon, A. Hauert, A. Jacot, and W. Kurz, *Metall. Mater. Trans.* **247A 38 A**, 1500 (2007).
- 248⁴ M. Gäumann, S. Henry, F. Cléton, J.-D. Wagnière, and W. Kurz, *Mater. Sci. Eng. A* **249271**, 232 (1999).
- 250⁵ Y. Amouyal, Z. Mao, C. Booth-Morrison, and D. N. Seidman, *Appl. Phys. Lett.* **94**, 25194 (2009).
- 252⁶ Y. Tu, Z. Mao, and D. N. Seidman, *Appl. Phys. Lett.* **101**, 28 (2012).
- 253⁷ A. Epishin, T. Link, U. Brückner, B. Fedelich, and P. Portella, in *Proceedings of the 254Tenth International Symposium on Superalloys* (Seven Springs, PA, 2004), pp. 537–255543.
- 256⁸ L. Felberbaum, K. Voisey, M. Gäumann, B. Viguier, and A. Mortensen, *Mater. Sci. Eng. A* **299**, 152 (2001).
- 258⁹ X. Do, D. Li, A. Zhang, B. He, H. Zhang, and T. Doan, *J. Laser Appl.* **25**, 2 (2013).
- 259¹⁰ M. Kunz, N. Tamura, K. Chen, A. A. MacDowell, R. S. Celestre, M. M. Church, S. 260Fakra, E. E. Domning, J. M. Glossinger, J. L. Kirschman, G. Y. Morrison, D. W. Plate, 261B. V. Smith, T. Warwick, V. V. Yashchuk, H. A. Padmore, and E. Ustundag, *Rev. Sci. 262Instrum.* **80**, (2009).
- 263¹¹ N. Tamura, in *Strain Dislocation Gradients from Diffraction. Spatially-Resolved 264Local Structure and Defects*, edited by R. Barabash, and G. Ice (World Scientific, 265London, 2014), pp. 125–155.
- 266¹² K. Chen, N. Tamura, W. Tang, M. Kunz, Y.C. Chou, K. N. Tu, and Y. S. Lai, *J. 267Appl. Phys.* **107**, 1 (2010).
- 268¹³ K. Chen, M. Kunz, N. Tamura, and H. -R. Wenk, *Geology* **43**, 219 (2015).
- 269¹⁴ A. Lupinacci, K. Chen, Y. Li, M. Kunz, Z. Jiao, G. S. Was, M. D. Abad, A. M. 270Minor, and P. Hosemann, *J. Nucl. Mater.* **458**, 70 (2015).
- 271¹⁵ K. Chen, N. Tamura, B. C. Valek, and K. N. Tu, *J. Appl. Phys.* **104**, 13513 (2008).
- 272¹⁶ Y. Li, L. Wan, and K. Chen, *J. Appl. Cryst.* **48**, 747 (2015).
- 273¹⁷ N. Siredey, M. Boufoussi, S. Denis, and J. Lacaze, *J. Cryst. Growth* **130**, 132 274(1993).
- 275¹⁸ See supplemental material at [URL inserted by AIP] for the distributions of crystal 276orientation of the substrate, Euler angles and rotation axes, peak position deviation, 277and residual strain in the substrate in Figure S1, S2, S3, and S4, respectively.

278¹⁹ B. C. Valek, N. Tamura, R. Spolenak, W. A. Caldwell, A. A. MacDowell, R. S.
279Celestre, H. A. Padmore, J. C. Bravman, B.W. Batterman, W. D. Nix, and J. R. Patel,
280J. Appl. Phys. **94**, 3757 (2003).
281²⁰ N. S. Hussein, D. P. Kumah, J. Z. Yi, C. J. Torbet, D. A. Arms, E. M. Dufresne, T.
282M. Pollock, J. Wayne Jones, and R. Clarke, Acta Mater. **56**, 4715 (2008).
283²¹ J. W. Aveson, P. A. Tennant, B. J. Foss, B. A. Shollock, H. J. Stone, and N. D'Souza,
284Acta Mater. **61**, 5162 (2013).
285²² J. Xue, A. Zhang, Y. Li, D. Qian, J. Wan, B. Qi, N. Tamura, Z. Song, and K. Chen,
286Sci. Rep., in press.

287

288TABLE I. Composition of DZ125L superalloy (wt. %)

Material	Co	Cr	W	Al	Ta	Ti	Mo	C	B	Ni
Substrate	9.54	8.74	6.46	5.03	3.96	3.18	2.21	0.12	0.0076	Balance
Powder	9.64	9.70	7.14	4.90	3.78	3.12	2.18	0.09	0.015	Balance

289

290 Figure Captions

291

292 FIG. 1. (a) Schematic and (b) optical microscopic image of the laser-assisted 3D
293 printed Ni-based superalloy deposited on the single crystalline substrate. (c)
294 Magnified image of the dendritic and stray grains of the region indicated by the red
295 rectangle in (b), and (d-e) the IPF maps along **Y**- and **X**-axis, respectively, obtained
296 from \square XRD. The {001} and {110} stereographic projection maps in (f-g) confirms
297 the single crystalline nature of dendritic grains (red poles) and non-preferred
298 orientation of stray grains (blue poles).

299

300 FIG. 2. Grain boundary distribution map in the \square XRD studied region, in which the
301 low angle grain boundaries in the dendritic region are delineated in the gradient of
302 light to dark red, while the high angle boundaries ($> 5^\circ$) are plotted in black.

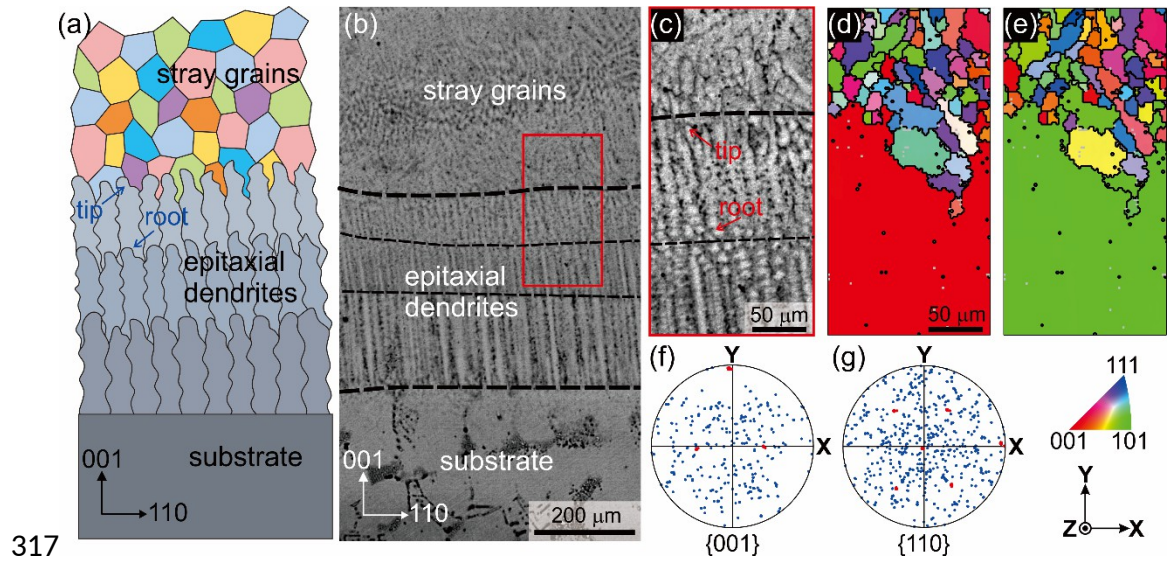
303

304 FIG. 3. (a) A magnified individual dendrite extracted from the rectangular region
305 highlighted in Figure 2 and (b) typical 133 Laue peaks along 3 lines of the dendrite
306 growth direction marked in (a), and (c) the distribution of disorientation gradient and
307 GND density along two lines parallel with the dendrite layer interface marked in
308 Figure 2. The GND density of the substrate is also shown as a comparison.

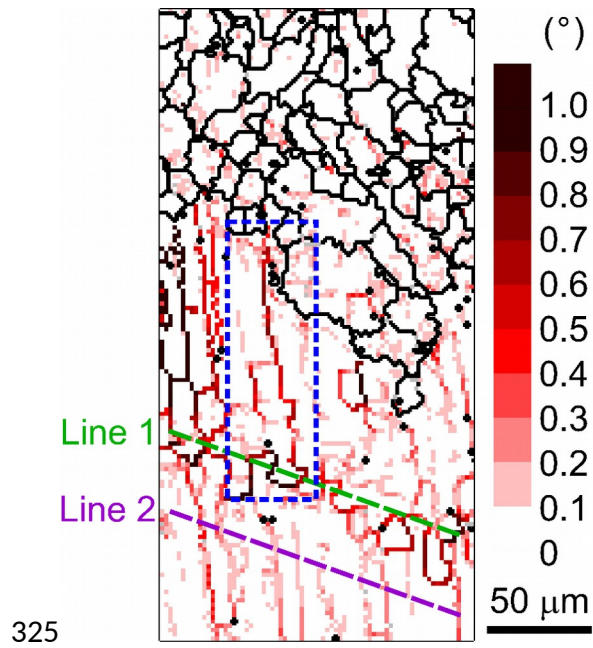
309

310 FIG. 4. Distribution maps of (a) von Mises strain, (b) compressive principal strain,
311 and (c) tensile principal strain. In (a) HAGBs and LAGBs are plotted in black and
312 blue, respectively. In (b-c) the interface between dendritic and stray grains are
313 displayed in black, and projections of the principal strain axes on **XY**-plane are
314 denoted by arrows in every 7th pixel. An arrow is plotted at the bottom right corner
315 to define the “fully in-plane” length.

316

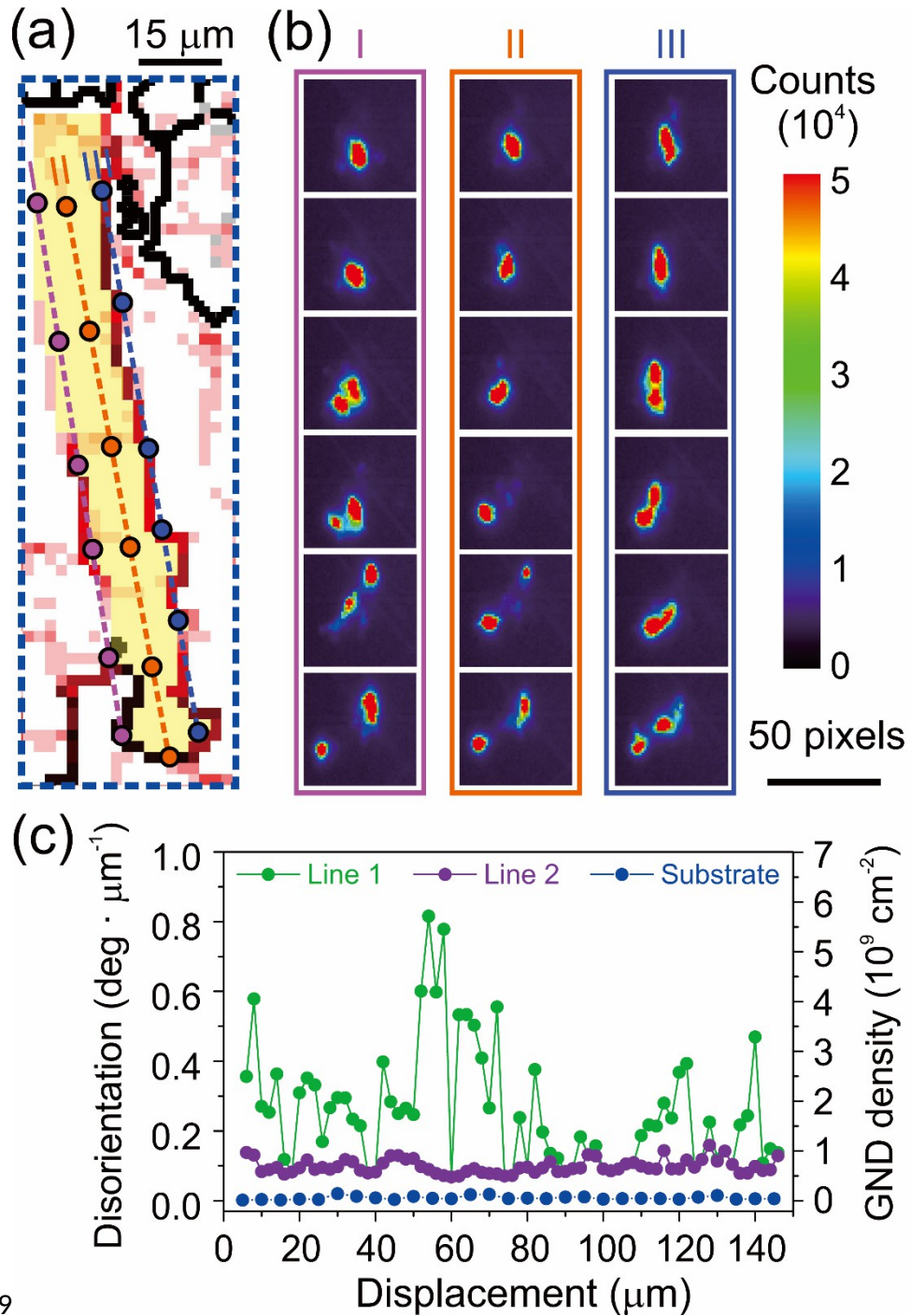


318 FIG. 1. (a) Schematic and (b) optical microscopic image of the laser-assisted 3D
 319 printed Ni-based superalloy deposited on the single crystalline substrate. (c)
 320 Magnified image of the dendritic and stray grains of the region indicated by the red
 321 rectangle in (b), and (d-e) the IPF maps along **Y**- and **X**-axis, respectively, obtained
 322 from \square XRD. The $\{001\}$ and $\{110\}$ stereographic projection maps in (f-g) confirms
 323 the single crystalline nature of dendritic grains (red poles) and non-preferred
 324 orientation of stray grains (blue poles).



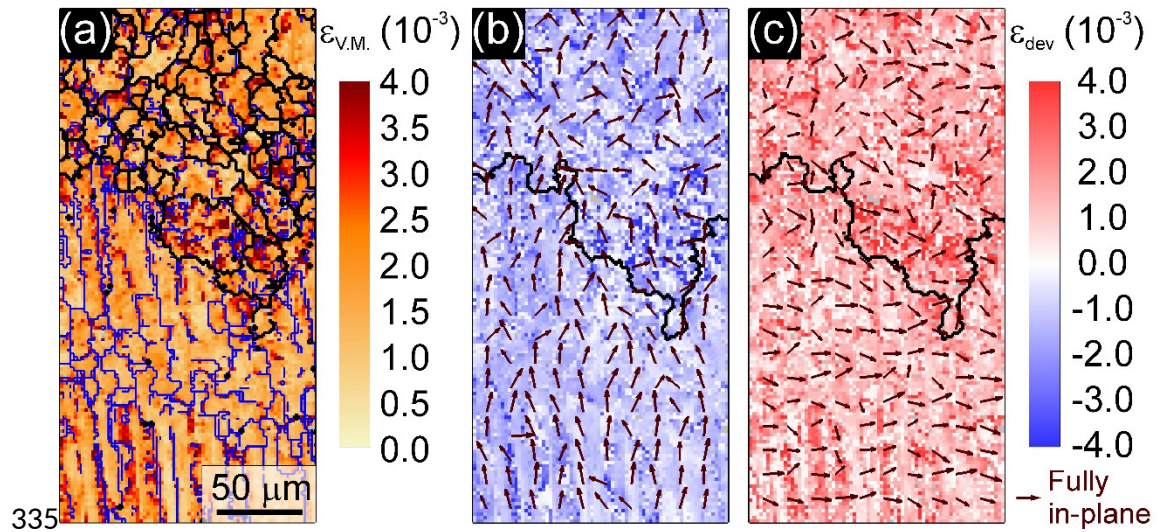
325

326 FIG. 2. Grain boundary distribution map in the XRD studied region, in which the
 327 low angle grain boundaries in the dendritic region are delineated in the gradient of
 328 light to dark red, while the high angle boundaries ($> 5^\circ$) are plotted in black.



329

330FIG. 3. (a) A magnified individual dendrite extracted from the rectangular region
 331highlighted in Figure 2 and (b) typical 133 Laue peaks along 3 lines of the dendrite
 332growth direction marked in (a), and (c) the distribution of disorientation gradient and
 333GND density along two lines parallel with the dendrite layer interface marked in
 334Figure 2. The GND density of the substrate is also shown as a comparison.



336 FIG. 4. Distribution maps of (a) von Mises strain, (b) compressive principal strain,
 337 and (c) tensile principal strain. In (a) HAGBs and LAGBs are plotted in black and
 338 blue, respectively. In (b-c) the interface between dendritic and stray grains are
 339 displayed in black, and projections of the principal strain axes on **XY**-plane are
 340 denoted by arrows in every 7th pixel. An arrow is plotted at the bottom right corner
 341 to define the “fully in-plane” length.